SEPTEMBER 2023
VOLUME 39, ISSUE 9

TAKE A LOOK INSIDE
Industry Briefs
—see page 14

KEY DATES
For a list of meetings
—see page 15

SPIE.
BACUS
PHOTOMASK TECHNOLOGY GROUP

The potential impact of artificial intelligence on the photomask industry

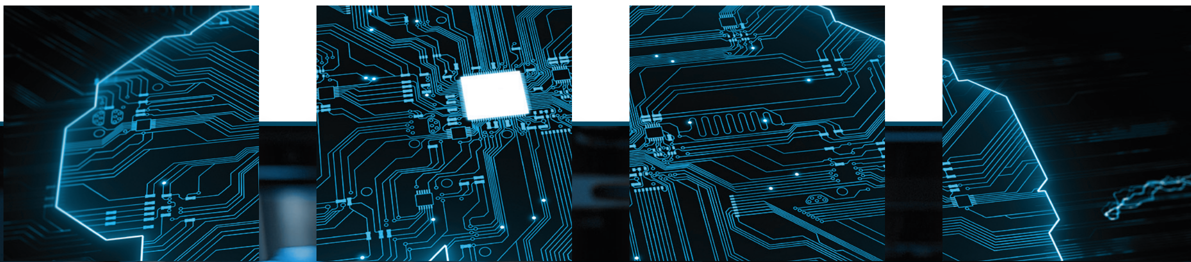

12293-23

EDITORIAL

The potential impact of artificial intelligence on the photomask industry

Anthony Vacca, *Automated Visual Inspection*

Artificial intelligence (AI) has emerged as a transformative technology across various industries, and the photomask industry is no exception. With its ability to analyze vast amounts of data, optimize complex processes, and enable new capabilities, AI is poised to significantly impact the photomask industry. Let's look at a few of the potential effects of AI on the industry, including improvements in design, inspection, and yield management.

Enhanced photomask design

AI may greatly improve photomask design by leveraging machine learning algorithms to analyze historical design data and identify patterns and correlations. By extracting insights from vast design databases, AI algorithms may assist in generating optimized layouts and predicting potential manufacturing issues. This could lead to improved design efficiency, reduced mask write time, and enhanced yield rates.

Furthermore, AI may also aid in the development of resolution enhancement techniques (RETs). By analyzing patterns, image quality, and process parameters, AI algorithms could potentially optimize RET algorithms, resulting in better pattern fidelity, reduced image distortions, and enhanced resolution.

Defect inspection and management

Defect review is a crucial aspect of photomask manufacturing. AI can play a pivotal role in automating and enhancing defect inspection and review processes. Machine learning algorithms can be trained on large datasets of defect images, enabling them to classify and identify defects with potentially high accuracy. This automation may not only increase inspection throughput by enabling automatic offline review but also reduce the risk of human error.

Moreover, AI may also contribute to defect management by analyzing defect data and potentially identifying root causes. By correlating defect information with process parameters and mask design data, AI algorithms may help in identifying systemic issues, enabling proactive defect prevention and mitigation strategies.

However, one major challenge exists in using AI for defect review in mask shops. Unlike wafer defect review, it is unacceptable for AI to misclassify even a single reticle defect that could cause killer repeating defects on the wafer. It will be interesting to see when and how AI technology will approach 100 percent accuracy in

BACUS News is published monthly by SPIE for BACUS, the international technical group of SPIE dedicated to the advancement of photomask technology.

Managing Editor/Graphics
Ty Binschus, *SPIE*

Exhibition and Sponsorship Coordinator:
Melissa Valum, *SPIE Sales Representative, Exhibitions and Sponsorships*

BACUS Technical Group Manager
Tim Lamkins, *SPIE*

2023 BACUS Steering Committee

President
Jed Rankin, *IBM Research*

Vice-President
Henry Kamberian, *Photronics, Inc.*

Secretary
Vidya Vaenkatesan, *ASML Netherlands BV*

Newsletter Editor
Artur Balasinski, *Infineon Technologies*

2023 Photomask Technology Conference Chairs
Ted Liang, *Intel Corp.*
Seong-Sue Kim, *Yonsei University*

Members at Large
Frank E. Abboud, *Intel Corp.*
Uwe F. W. Behringer, *UBC Microelectronics*
Ingo Bork, *Siemens EDA*
Tom Cecil, *Synopsys, Inc.*
Brian Cha, *Entegris Korea*
Aki Fujimura, *D2S, Inc.*
Emily Gallagher, *imec*
Jon Haines, *Micron Technology Inc.*
Bryan Kasprowicz, *HOYA*
Romain J Lallement, *IBM Research*
Takaharu Nagai, *Dai Nippon Printing*
Kent Nakagawa, *Toppan Photomasks, Inc.*
Patrick Naulleau, *EUV Tech, Inc.*
Jan Hendrik Peters, *bmbg consult*
Steven Renwick, *Nikon*
Douglas J. Resnick, *Canon Nanotechnologies, Inc.*
Thomas Scheruebl, *Carl Zeiss SMT GmbH*
Ray Shi, *KLA Corp.*
Anthony Vacca, *Automated Visual Inspection*
Michael Watt, *Shin-Etsu MicroSi Inc.*
Larry Zurbrick, *Keysight Technologies, Inc.*

P.O. Box 10, Bellingham, WA 98227-0010 USA
Tel: +1 360 676 3290
SPIE.org
help@spie.org
©2023

SPIE.

SPIE is a registered trademark of the Society of Photo-Optical Instrumentation Engineers.
All rights reserved.

determining false defects from killer defects. In the meantime, human review of AI classifications will be needed.

Quality control and yield improvement

AI's data analysis capabilities may also aid in real-time quality control during the photomask manufacturing process. By monitoring and analyzing data from various inspection and metrology tools, AI algorithms could identify deviations or anomalies, enabling prompt corrective actions. This proactive approach may minimize defects and enhance yield rates.

Artificial intelligence has the potential to greatly improve the photomask industry by enhancing design, improving write/inspection throughput, and driving yield improvement. As AI technologies continue to evolve, the photomask industry may leverage its capabilities to achieve higher productivity, better quality control, and faster time-to-market for semiconductor devices.

SPIE. BACUS PHOTOMASK TECHNOLOGY GROUP

BACUS News is published monthly by SPIE for BACUS, the international technical group of SPIE dedicated to the advancement of photomask technology.

Managing Editor/Graphics
Ty Binschus, *SPIE*

Exhibition and Sponsorship Coordinator:
Melissa Valum, *SPIE Sales Representative, Exhibitions and Sponsorships*

BACUS Technical Group Manager
Tim Lamkins, *SPIE*

2023 BACUS Steering Committee

President
Jed Rankin, *IBM Research*

Vice-President
Henry Kamberian, *Photronics, Inc.*

Secretary
Vidya Vaenkatesan, *ASML Netherlands BV*

Newsletter Editor
Artur Balasinski, *Infineon Technologies*

2023 Photomask Technology Conference Chairs
Ted Liang, *Intel Corp.*
Seong-Sue Kim, *Yonsei University*

Members at Large
Frank E. Abboud, *Intel Corp.*
Uwe F. W. Behringer, *UBC Microelectronics*
Ingo Bork, *Siemens EDA*
Tom Cecil, *Synopsys, Inc.*
Brian Cha, *Entegris Korea*
Aki Fujimura, *D2S, Inc.*
Emily Gallagher, *imec*
Jon Haines, *Micron Technology Inc.*
Bryan Kasprowicz, *HOYA*
Romain J Lallement, *IBM Research*
Takaharu Nagai, *Dai Nippon Printing*
Kent Nakagawa, *Toppan Photomasks, Inc.*
Patrick Naulleau, *EUV Tech, Inc.*
Jan Hendrik Peters, *bmbg consult*
Steven Renwick, *Nikon*
Douglas J. Resnick, *Canon Nanotechnologies, Inc.*
Thomas Scheruebl, *Carl Zeiss SMT GmbH*
Ray Shi, *KLA Corp.*
Anthony Vacca, *Automated Visual Inspection*
Michael Watt, *Shin-Etsu MicroSi Inc.*
Larry Zurbrick, *Keysight Technologies, Inc.*

P.O. Box 10, Bellingham, WA 98227-0010 USA
Tel: +1 360 676 3290
SPIE.org
help@spie.org
©2023

SPIE.

SPIE is a registered trademark of the Society of Photo-Optical Instrumentation Engineers.
All rights reserved.

FEATURED ARTICLE

A study of patterning 36nm-pitch logic contact holes in a metal oxide resist using a high-reflectance phase-shifting mask that results in image reversal

Shih-En Tseng, *ASML TDC (Taiwan);* **Chun-Kuang Chen,** *ASML TDC (Taiwan);* **Dong-Seok Nam,** *ASML Technology Development Center (USA);* **Will Lin,** *ASML TDC (Taiwan);* **Anthony Yen,** *ASML Technology Development Center (USA)*

ABSTRACT

High-reflectance phase-shifting mask (HR-PSM) is studied for patterning 36nm-pitch logic contact holes and compared with other mask absorbers in terms of imaging performance (ILS, LCDU, MEEF, etc.) and exposure dose. To this end, wafer-data-calibrated EUV resist models for CAR and MOR are used. Our simulation results show that a HR-PSM produces dark-field images at large mask CD. However, as mask CD decreases, the tone of the images is reversed and bright-field images of good contrast can be generated. Based on this observation, a HR-PSM plus MOR patterning approach is proposed for through-pitch logic contact hole applications with a minimum pitch equal to 36 nm. We show that this approach demonstrates multiple enhancements in terms of through-pitch performance and enables us to extend the practical resolution of logic contact holes below the pitch of 40 nm using the 0.33NA EUV scanner.

INTRODUCTION

EUV lithography has been successfully implemented in high volume manufacturing at logic 7- and 5-nm nodes. As design rules continue to shrink, one of the challenges of patterning logic contact holes below the 40-nm pitch is the trade-off between imaging performance and wafer patterning cost. As shown in the left graph of Figure 1, traditionally for such applications, a dark-field TaBN-based binary mask is used to create contact holes in a positive-tone chemically amplified resist (CAR). On the contrary, a bright-field binary mask will be necessary to create holes in a negative-tone resist such as a metal oxide resist (MOR). The former approach (dark-field TaBN mask plus CAR) may require higher exposure dose to reduce local critical-dimension uniformity (LCDU) and hence may not be cost-effective. Although the latter approach (bright-field TaBN mask plus MOR) benefits from the lower resist blur of MOR, it bears the risk of printing of embedded phase defects in the mask blank.

Attenuated phase-shifting masks (PSM) in EUV lithography have been extensively studied to improve imaging performance[1-5]. In particular, Ahn[5] proposed a high-reflectance phase-shifting mask (HR-PSM) for contact-hole patterning to achieve better performance than traditional binary masks by optimizing the shifter's thickness in terms of NILS, MEEF, dose, and LCDU and minimizing the sensitivity to mask and lithography process variations. However, it is noteworthy that all these PSM-based patterning approaches result in bright light exposing a positive-tone resist to print holes directly in the resist.

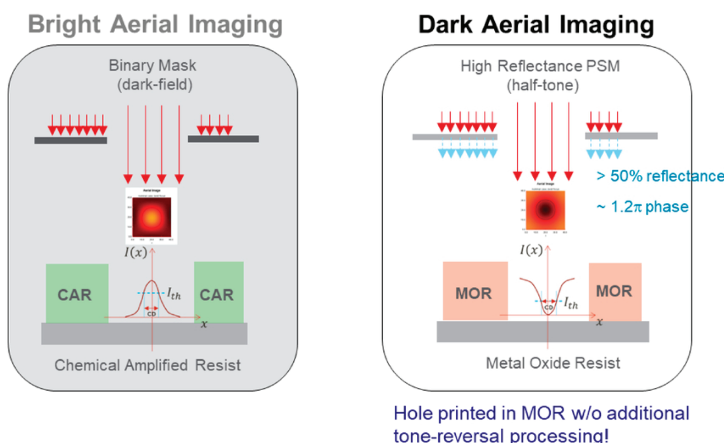

Figure 1. *The left graph illustrates that a dark-field binary mask creates a contact hole in a positive-tone CAR whereas the right graph shows that a half-tone HR-PSM reverses the tone of the image and generates a hole in a negative-tone MOR.*

To overcome the drawbacks of these approaches, or in other words, to combine the advantages of HR-PSM and MOR, we propose a novel solution that will result in more favorable (tighter) LCDU by reversing the tone of the image at the wafer plane in combination with

a negative-tone MOR to form holes at small pitches without the additional tone-reversal process[6], as illustrated in the Figure 1 graph. Based on wafer-data-calibrated resist models, we will assess the through-pitch image performance of our approach (HR-PSM+MOR) for logic contact holes with a 36-nm minimum pitch and demonstrate multiple enhancements against other mask absorbers in low-k1 imaging, enabling us to extend the practical resolution of logic contact holes to below the 40-nm pitch using the 0.33NA EUV scanner.

In the remaining sections of this paper, we will first describe the physics of tone reversal in aerial image in Section 2, then derive in Sections 3 and 4 a simple LCDU model for EUV contact holes and calibrate the resist models based on wafer data of CAR and MOR. In Section 5, based on the calibrated resist models, we will assess the through-pitch imaging performance of HR-PSM for logic contact holes against other mask absorbers. As a conclusion of this work, we will summarize the benefits and drawbacks of our proposal, and identify and project its application limit for 0.33NA EUV scanners.

PHYSICS OF TONE REVERSAL IN AERIAL IMAGE

The idea of tone reversal in aerial image is well known in the use of alternating PSM (AltPSM) and chromeless PSM. Even a completely bright mask can generate dark features in the image if phase shifts are present in the transmitted or reflected light[1]. Chromeless PSM contains no absorber on it and π-phase shifters are realized by etching into the mask substrate. In contrast, the HR-PSM we propose uses a high-transmission absorber whose thickness is optimized to achieve a relative reflectance higher than 50%.

In this section, we will first describe the physics of tone reversal in aerial image for a 1D mask based on the Kirchhoff theory. We will then demonstrate the phenomenon of image tone reversal for contact holes using 3D mask simulation by varying mask CD on HR-PSM and other mask absorbers.

Physics of tone reversal in aerial image for a 1D mask

We begin with a simple description of the physics of tone reversal in the aerial image. The same phenomenon was taken advantage of in optical lithography quite some time ago[1-2]. In our simple treatment, we study a 1D mask with two phase edges with the mask transmission function *M* in the left graph of Figure 2.

For treating 1D cases, the point-spread function of the imaging system can be simplified to $h(x) = sinc\left(\frac{2NA}{\lambda}x\right)$. And the optical disturbance *U*(*x*) in the wafer plane is the convolution of the mask transmission function and the point-spread function; that is,

$$U(x) = \int_{-\infty}^{\infty} M(x')h(x-x')\,dx' = \frac{1}{\sqrt{2}}\int_{-\infty}^{-\epsilon} h(x-x')\,dx' - \int_{-\epsilon}^{\epsilon} h(x-x')\,dx' + \frac{1}{\sqrt{2}}\int_{\epsilon}^{\infty} h(x-x')\,dx'$$
$$= \frac{1}{\sqrt{2}}\int_{-\infty}^{\infty} h(x-x')\,dx' - \frac{2+\sqrt{2}}{2}\int_{-\epsilon}^{\epsilon} h(x-x')\,dx' = -\frac{1}{\sqrt{2}}\int_{\infty}^{-\infty} h(\eta)\,d\eta + \frac{2+\sqrt{2}}{2}\int_{x+\epsilon}^{x-\epsilon} h(\eta)\,d\eta$$
$$= \frac{\lambda}{2\sqrt{2}NA} - \frac{2+\sqrt{2}}{2}\int_{x-\epsilon}^{x+\epsilon} h(\eta)\,d\eta,$$

where we made use of the definite integral

$$\int_{-\infty}^{\infty} h(\eta)\,d\eta = \int_{-\infty}^{\infty} sinc\left(\frac{2NA}{\lambda}\eta\right)d\eta = \frac{\lambda}{2NA}\int_{-\infty}^{\infty}\frac{\sin \pi y}{\pi y}\,dy = \frac{\lambda}{2NA}\cdot 1$$

If |*x*| is very large, then the second integral is zero, and $U(\pm\infty) = \frac{\lambda}{2\sqrt{2}NA}$. This means that far from the phase edges, the mask behaves simply like a usual semi-transparent mask.

If ϵ is relatively large, then at |*x*| = ϵ,

$$U(\pm\epsilon) = \frac{\lambda}{2\sqrt{2}NA} - \frac{2+\sqrt{2}}{2}\int_{0}^{2\epsilon} h(\eta)\,d\eta \approx \frac{\lambda}{2\sqrt{2}NA} - \frac{2+\sqrt{2}}{2}\int_{0}^{\infty} sinc\left(\frac{2NA}{\lambda}\eta\right)d\eta$$
$$= \frac{\lambda}{2\sqrt{2}NA} - \frac{2+\sqrt{2}}{2}\cdot\frac{\lambda}{4NA} = -0.21\times\frac{\lambda}{2\sqrt{2}NA}$$

Since *U*(*x*) must be a continuous function, it must cross the horizontal axis somewhere between |*x*| = ∞ and |x| = ϵ, and because the negative value is rather small, we should have two points of zero intensity somewhere close to |x| = ϵ. At x = 0, we carry out the integral as follows:

$$U(0) = \frac{\lambda}{2\sqrt{2}NA} - \frac{2+\sqrt{2}}{2}\int_{-\epsilon}^{\epsilon} h(\eta)\,d\eta = \frac{\lambda}{2NA}\left(\frac{1}{\sqrt{2}} - \frac{2+\sqrt{2}}{2}\int_{-\delta}^{\delta}\frac{\sin \pi y}{\pi y}\,dy\right)$$

where $\delta = \frac{2NA}{\lambda}\epsilon$. For a relatively large ϵ, $\int_{-\infty}^{\infty}\frac{\sin \pi y}{\pi y}dy = 1$ and $U(0) = -\frac{\lambda}{2NA}$. We now divide all values by $\frac{\lambda}{2NA}$, we then have the normalized $U(\pm\infty) = \frac{1}{\sqrt{2}}$ and $U(0) = -1$, same as the values of the mask transmission function at these points.

FEATURED ARTICLE

If ϵ is not large, then, when normalized,

$$U(0) = \frac{1}{\sqrt{2}} - \frac{2+\sqrt{2}}{2\pi}\int_{-\delta}^{\delta}\frac{\sin \pi y}{\pi y}dy$$

We can see that $U(0)$ approaches zero as the term with the integral becomes very small, when δ gets very small, resulting in a very low image intensity at x = 0, as shown in the Fig. 2 graph. Setting $U(0) = 0$, we get $\int_{-\delta}^{\delta}\frac{\sin \pi y}{\pi y}dy \approx$ 0.42. This means we can approximate the integral simply as $\frac{\sin 0}{0}\cdot 2\delta$, which gives $\delta = 0.21$ and $2\epsilon = \delta \times \frac{\lambda}{NA} = 0.21 \times \frac{13.5}{0.33} = 8.6\ \mathrm{nm}$.

Figure 2 gives the simulated results of normalized intensity $|U(x)|^2$ of such a mask with various slit widths. Tone reversal in aerial image occurs with slit width smaller than 10 nm (wafer, not mask, dimension) based on thin mask assumption.

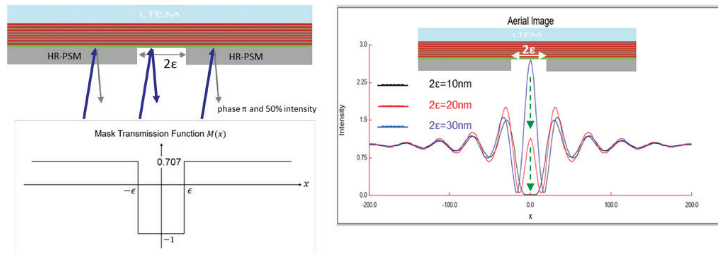

Figure 2. *The mask transmission function of a high-transmission phase-shift mask with a slit width equal to 2ε (left). In the right graph, a Kirchhoff mask of relative transmission of 50% and a phase shift of 1.0π is simulated. Tone reversal in aerial image occurs with slit width smaller than 10 nm (wafer, not mask, dimension).*

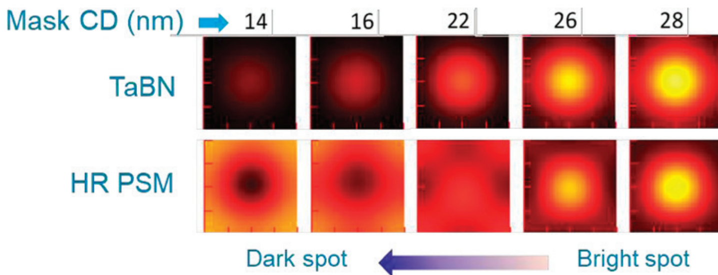

Figure 3. *Different from the response of TaBN mask, HR-PSM reverses the image of the hole pattern from a bright spot to a dark spot as mask CD becomes smaller and smaller.*

Image tone reversal of contact holes for HR-PSM

The above phenomenon of HR-PSM for 1D lines and spaces can be extended to 2D contact hole patterns and the aerial images for the absorbers studied will be simulated assuming a 3D mask structure. Figure 3 gives an example of aerial images of 40nm-pitch contact holes by decreasing mask CD on HR-PSM and TaBN absorbers. It demonstrates that HR-PSM responds differently from TaBN and that as mask CD decreases from 28 nm to 14 nm (at the wafer dimension), the image of hole patterns is reversed from a bright spot to a dark spot.

DERIVATION OF LCDU MODEL FOR EUV CONTACT HOLES

As stated previously, our approach is to couple the bright-field image of HR-PSM with low resist blur of negative-tone MOR. We have demonstrated in Section 2 that by decreasing the mask CD, the image tone of HR-PSM can be reversed to result in a bright-field image of good contrast. Next, we derive an LCDU model for contact holes which is simple and accurate enough to describe the image behaviors of MOR around practical operation conditions.

As device dimensions continue to shrink with EUV lithography, stochastic noise is getting more and more serious such that lots of works[7-13] about LCDU and/or LWR have been presented in order to model and/or mitigate their impact on device performance.

The basis of many of the LWR/LCDU models[9,11-13] is to translate the dose fluctuation to edge placement variation based on quantum statistics. However, different definitions of effective area element finally lead to model variants of different forms. For instance, from dose fluctuation and Poisson's statistics, Bernd Geh[12] derived a 3σ-LCDU model as follows:

$$LCDU = \frac{6}{ILS}\sqrt{\frac{h\nu}{Dose\cdot\Delta A}}$$

This equation includes an area element ΔA where the photon number is counted and LCDU is measured from. By choosing CD^2 as area element and introducing a constant k_4, the above model becomes

$$LCDU = \frac{k_4}{NILS}\sqrt{\frac{h\nu}{Dose}}$$

FEATURED ARTICLE

where the k_4-factor can be a measure of resist performance such as blur, absorption, and quantum efficiency and a *NILS* of blurred aerial image is used. This model indicates that LCDU is inversely proportional to CD and blurred ILS.

On the basis of Geh's work[12], Santaclara et al.[13] further decomposes the LWR model for lines and spaces into three material contributors: absorption and quantum efficiency, resist blur, and dose-to-clear (D2C), as

$$LWR_{3\sigma,unb} = k_4 \cdot e^{\left(\frac{\sqrt{2}\pi\sigma}{p}\right)^2} \sqrt{\frac{hv}{D_{thr}}} \frac{1}{ILS}$$

chemistry (QE, α) blur pitch Dose to clear

In the above equation, k_4 is a new factor which is a function of absorption and quantum efficiency without any dependency of resist blur.

It is noteworthy to emphasize that the LCDU model we describe in this section belongs to one of such models which turn the stochastic dose fluctuation into CD variation. However, the area element is defined differently as explained below.

Based on the threshold resist model, for a feature exposed at a given focal plane, the correlation between the exposure dose and the aerial image intensity threshold can be described by the following formula[9,11]:

$$D2C = E_{op} \times I_{th} \tag{1}$$

where *D2C* denotes the dose-to-clear for positive-tone resist or the dose-to-gel (*D2G*) for negative-tone resist, E_{OP} is the dose required to print the feature on target and I_{th} is the normalized intensity threshold of blurred aerial image. Taking the derivative on both sides of Eq. (1) and after re-arrangement, we have the stochastic dose fluctuation ($\delta E_{op}/E_{op}$)

$$\frac{\delta E_{op}}{E_{op}} = -\frac{\delta I_{th}}{I_{th}} = \frac{1}{I_{th}}\left|\frac{\partial I_{th}}{\partial x}\right| \delta x = bILS \cdot \delta x \tag{2}$$

where *bILS* is the blurred image log slope under the presence of resist blur:

$$bILS \equiv \frac{\partial \ln(I_{th})}{\partial x} = \frac{1}{I_{th}}\frac{\partial I_{th}}{\partial x} \tag{3}$$

The feature edge variation δx can then be expressed as functions of *bILS* and $\delta E_{op}/E_{op}$:

$$\delta x = \frac{1}{bILS}\frac{\delta E_{op}}{E_{op}} \tag{4}$$

From quantum statistics, dose fluctuation being proportional to the variation of the photon number ($\sqrt{N}/N$) in one standard deviation σ_N, we get

$$\frac{\Delta E_{op}}{E_{op}} \propto \frac{\sqrt{\langle N\rangle}}{\langle N\rangle} = \frac{1}{\sqrt{\langle N\rangle}} = \sigma_N \tag{5}$$

Combining Eq. (4) and (5), we have the stochastic edge roughness in three standard deviations as follows.

$$3\sigma_N \propto \frac{1}{bILS}\frac{3\sigma_E}{\langle E_{op}\rangle} = \frac{3\sigma_N}{bILS} = \frac{3}{bILS}\frac{1}{\sqrt{\langle N\rangle}} \tag{6}$$

where $\langle N\rangle$ is the average number of photons absorbed by the feature. Alternatively, by introducing a stochastic coefficient *k*, Eq. (6) can be generalized to the form below:

$$3\sigma_N = \frac{3k}{bILS}\frac{1}{\sqrt{\langle N\rangle}} \tag{7}$$

Eq. (7) can be used to characterize the "line edge roughness (LER)" for lines and spaces (LS) or "contact edge roughness (CER)" for contact holes (CH), where the coefficient *k* needs to be calibrated from wafer data. Assuming both edges of a metrology cutline are stochastically un-correlated, the CD variation can therefore be calculated as the quadratic sum of Eq. (7), that is,

$$3\sigma_{CD} = \frac{3\sqrt{2}k}{bILS}\frac{1}{\sqrt{\langle N\rangle}} \tag{8}$$

Eq. (8) is named as the "line width roughness (LWR)" and "local CD uniformity (LCDU)" for LS and CH, respectively.

So far our approach is the same as that of Geh. However, the subsequent choice of area element as well as its definition of area δA_i or ΔA will make a difference in the final model. Here in our model the photon number is calculated as follows.

$$\langle N \rangle = \frac{D2C \times \langle \delta A_i \rangle}{h\nu} \quad (9)$$

For LS features, δA_i is considered a small metrology area element along the line and can be written as

$$\delta A_i = \frac{CD}{2} \times \delta y_i = \frac{CD_i}{2} \quad (10)$$

where the unit length of metrology segment $\delta y_i = 1$ nm is assumed. Or statistically, we can average all sampled segments CD_i

$$\langle \delta A_i \rangle = \frac{\langle CD_i \rangle}{2} = CD/2 \quad (11)$$

Similarly, for a contact hole array, we have

$$\delta A_i = \frac{1}{2} r_i \times r_i \delta\theta_i = \frac{CD_i}{4}$$

or

$$\langle \delta A_i \rangle = \frac{\langle CD_i \rangle}{4} = CD/4 \quad (12)$$

where δA_i is a small portion of a hole circle and the unit length of metrology segment $r_i \delta\theta_i = 1$ nm is assumed. Substituting Eq. (11) and Eq. (12) for $\langle \delta A_i \rangle$ in Eq. (9), we get from Eq. (8)

$$LWR \text{ or } LCDU = \frac{k}{\sqrt{D2C} \times \sqrt{CD} \times bILS} \quad (13)$$

Here the coefficient k combines all the constants in Eq. (8) to Eq. (12). Different from the k_4's[12,13], Eq. (13) shows that LWR and LCDU are inversely proportional to $\sqrt{CD}$ rather than CD. It also implies that the reduction of LWR and LCDU requires improving the image quality, *bILS*, and/or increasing the photon number contained in the feature through higher D2C and larger wafer CD size. Also, our purpose is different; k in Eq. (13) is used in the modeling of LWR or LCDU of a particular resist; we do not look to compare LWR or LCDU performance of various resists, as k_4, as a proposed metric, is meant to do.

CALIBRATION OF RESIST MODELS FOR CAR AND MOR RESISTS

Once LCDU and LWR models are available, we can calibrate these models using silicon data to obtain critical resist properties such as dose sensitivity, resist blur, stochastic coefficient k, etc.

Model calibration for CAR

Two types of resist data sets are used for calibration in this section: CAR for CH and MOR for LS. The first dataset is for staggered CH array exposed with 0.33NA EUV hexapoles in positive-tone CAR resist. The minimum pitches are 40 nm and 44 nm with a few splits in dimension on mask (DOM) for each pitch. Then wafer CD and LCDU are measured for all exposure conditions.

From threshold resist model Eq. (1), we have D2C ≈ 10 mj/cm^2 with a 4-nm resist blur best matched to multiple DOM wafer CD data over the full dose range for this CAR resist, as shown in the top two graphs of Figure 4. On the other hand, the bottom two graphs show that our model fails to predict the trend-up of LCDU for higher doses but matches well with wafer LCDU for lower doses. Part of the reason is that our LCDU model is derived from stochastic dose variation only, without taking into account photon absorption and quantum efficiency of acid generation[9,10]. This partial matching to wafer LCDU also provides an evidence that photon counting would be adequate to depict the LCDU performance of small holes.

As a result, the stochastic coefficient k ≈ 3.6 is achieved on average for through-pitch CH exposed in CAR. Depending on the pitch and DOM, the LCDU models predict well wafer data when holes' dimension on wafer (DOW) ≤ half-pitch (HP) + 2 nm. In other words, the prediction of such calibrated models will be sufficiently accurate if the target CD on wafer is kept within this range of validity.

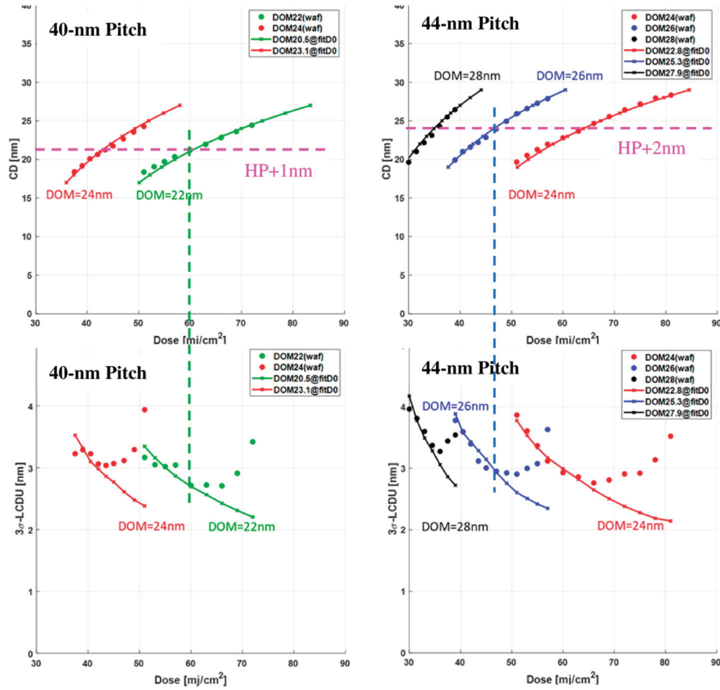

Figure 4. Resist model calibration for staggered contact holes exposed in CAR using EUV 0.33NA with hexapole illumination. These plots show matching between our simulation prediction and measured wafer data for CD (top row) LCDU (bottom row) through dose. CH pitches are 40 nm (left column) and 44 nm (right column). Dot points indicate wafer data, "x" points with solid lines are model-predicted data that best fit D2C and DOM. The vertical dashed lines represent the dose limits below which LCDU model fits best wafer data. This limit is associated to wafer CD limit as indicated by the horizontal pink dashed line.

Model calibration for MOR

The second model calibration is for LS feature illuminated with 0.33NA EUV dipoles in negative-tone MOR. The minimum pitches are 32 nm and 28 nm with equal lines and spaces. Then wafer CD and LCDU are measured for a full field focus-exposure dose matrix (FEM).

Figure 5 shows a good fit of model calibration to wafer CD-based FEM and a good match of CD through dose at best focus for 32nm-pitch LS exposed in MOR. The calibration results in dose-to-gel (D2G) = 16.5 mj/cm^2, resist blur ≈ 2 nm with estimated mask CD = 15.6 nm, which proves the lower image blur of MOR vs. CAR. The process window of the model showing a good match at best focus (BF) covers 52% EL and 80 nm depth of focus (DOF). The corresponding CD range at BF is larger than HP + [-2,2] nm. The maximum CD deviation is 0.36 nm within the field of calibration. It is noteworthy to mention that the practical operation conditions in the fab is well within this process window with large enough process tolerance such that we believe our calibrated model is accurate enough to predict CD response for MOR.

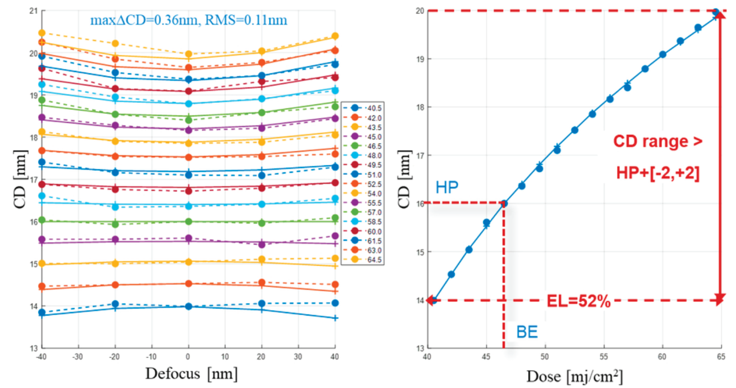

Figure 5. Resist model calibration for 32nm-pitch LS exposed in MOR using EUV 0.33NA with dipole illumination. In the left plot, dot-dashed lines indicate wafer FEM data and the corresponding solid lines are model-predicted data. The right plot shows a good matching of CD resist model through dose at best focus.

The same calibration approach is applied to 28nm-pitch LS exposed with an optimal dipole illumination. As shown in Figure 6, same resist properties fit well to the wafer data of 28nm-pitch LS with MOR, D2G = 16.5 mj/cm^2, resist blur ≈ 2 nm with estimated mask CD = 13.7 nm. The maximum CD deviation is 0.31 nm within the calibration field. The calibrated model remains valid within a process window of 64% EL and 60nm-DOF. The corresponding CD range at BF is HP + [-3,3] nm.

We have also calibrated our LWR model (Eq. 13) to match LWR-based FEM for 32nm-pitch and 28nm-pitch LS with MOR, which shows LWR is simply inversely proportional to bILS and the square root of *D2G* and DOW. However, in order to better match the wafer data, we have to introduce an LWR offset and modify Eq. 13 as follows

$$LWR = \frac{k}{\sqrt{D2C} \times \sqrt{CD} \times bILS} + LWR_{offset} \qquad (14)$$

This equation implies that there is always some intrinsic LWR even when the bILS goes to infinity[7]. The fitting quality of LWR vs. dose at BF is shown in Figure 7. The calibration of LWR model for LS of both pitches results in the stochastic coefficient $k \approx 2.7$ and $LWR_{offset} \approx 3$ nm for MOR.

As a summary of this section, based on wafer data, we suggest the following resist parameters for further assessment, as shown in Table 1.

resist type	D2C or D2G (mj/cm²)	resist blur (nm)	stochastic coefficient (k)	LCDU or LWR offset (nm)	model valid CD (nm)
CAR	10	4	3.6	~ 0	CD ≤ HP+2
MOR	16.5	2	2.7	3	CD ≤ HP+3

Table 1. Key parameters of resist models calibration for CAR and MOR.

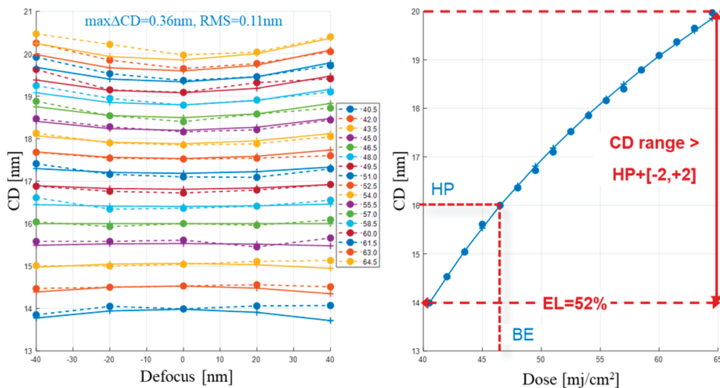

***Figure 6.** Resist model calibration for 28nm-pitch LS exposed in MOR using EUV 0.33NA with dipole illumination. In the left plot, dot-dashed lines indicate wafer FEM data and the corresponding solid lines are model-predicted data. The right plot shows a good matching of CD resist model through dose at best focus.*

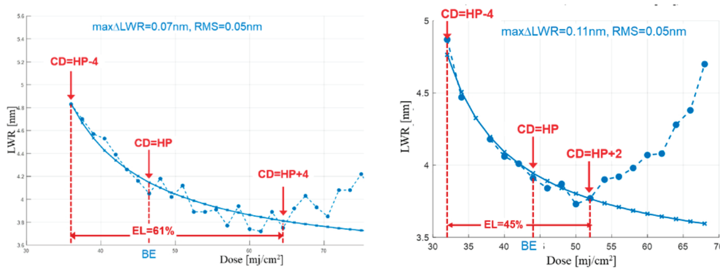

***Figure 7.** LWR model calibration at best focus for 32nm- (left) and 28nm-pitch (right) LS for MOR.*

IMAGING PERFORMANCE OF HR-PSM AGAINST EXISTING ABSOBERS FOR 36-NM-PITCH LOGIC CONTACT HOLES

We have characterized the essential properties of EUV resists for CAR and MOR in the previous section. In this section, based on the above calibrated models, we compare HR-PSM and existing mask absorbers, evaluate their imaging performance for single patterning of logic contact holes with 36nm-minimum pitch, and identify the best application domains for different absorbers.

The optical properties of three types of absorbers are listed in Table 2. The TaBN-based mask is the baseline of current industry technology for hole patterning while Gao et al.[11] have shown that low-n high-k (LnHk) mask offers certain benefits in contrast, through-pitch best focus shift, and dose for metal layers. These two types of masks producing bright holes work with a positive-tone resist (CAR) whose D2C = 10 mj/cm² and resist blur = 4 nm are assumed in the simulation assessment of lithographic metrics. On the contrary, the Mo-based HR-PSM generates dark holes in a negative-tone resist (MOR) where D2G = 16.5 mj/cm² and resist blur = 2 nm are used.

LCDU and exposure dose determination at 36nm-min pitch CH

Considering the need of balanced performance through pitch, an annular illumination with σ = [0.55,0.85] is selected to expose 36nm-min pitch CH with 0.33NA. For a given target CD, the intensity threshold I_{th} and its associated blurred ILS of CH are simulated as a function of mask CD for every pitch. LCDU and exposure dose can then be calculated from Eq.(1) and (13). As a result, the LCDU vs. dose correlation for all three absorbers are plotted as illustrated in Figure 8. The target CD here is set to be 20 nm. This selection respects the application rule of the calibrated LCDU models, CD ≤ HP + 2 nm such that a sufficient accuracy of the resist models to predict the imaging performance can be ensured. Besides, it is noteworthy to remember that because of different image tones, TaBN and LnHk absorbers are associated with CAR and HR-PSM absorber with MOR, respectively. The related resist parameters are listed in Table 1.

Figure 8 demonstrates that for 36nm-min pitch CH, there exists a certain dose range between min. LCDU of HR-PSM (red dashed line) and that of LnHk (black dashed line), where HR-PSM can achieve lower LCDU than TaBN and LnHk absorbers. In other words, below some LCDU threshold, single patterning of CH can only be implemented by HR-PSM absorber.

Comparison of lithographic metrics through pitch

Assuming LCDU requirement is 10% of the target CD, that is, LCDU ≤ 2 nm, the exposure dose needed for

Absorber	Mask	n	k	t (nm)	Reflectance	phase (π)
TaBN	POR	0.95	0.031	60	2.6%	0.99
LnHk	weak PSM	0.909	0.053	39	3.1%	1.18
Molybdenum	HR-PSM	0.9237	0.0064	53	55%	1.23

Table 2. *Three absorbers studied for comparison of imaging performance for logic contact hole through-pitch.*

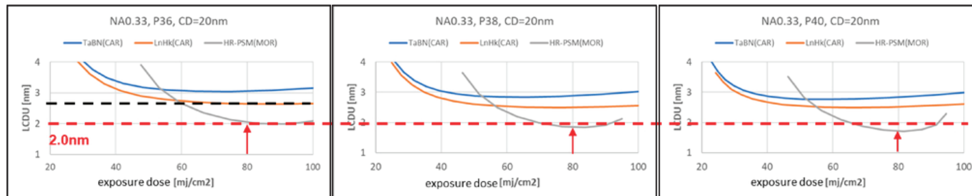

Figure 8. *At target CD = 20nm, LCDU is calculated as a function of exposure dose for CH with pitches 36 nm, 38 nm and 40 nm exposed with 3 mask absorbers.*

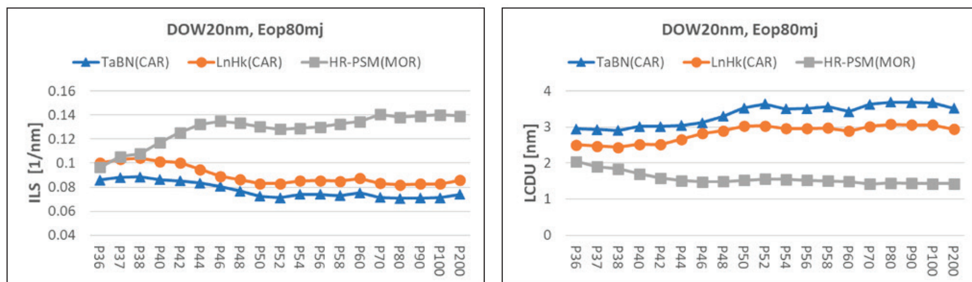

Figure 9. *Comparison of through-pitch blurred ILS (left) and LCDU (right) for 3 mask absorbers.*

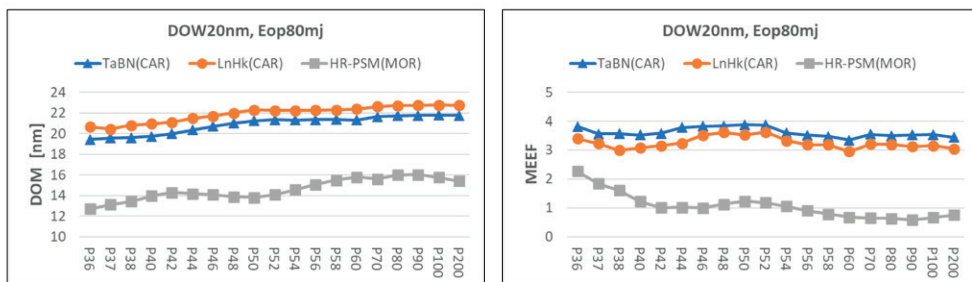

Figure 10. *Comparison of through-pitch 1X DOM (left) and MEEF (right) for 3 mask absorbers. DOM is optimized by simple mask CD biasing. No sub-resolution assist features is used.*

36nm-pitch CH is about 80 mj/cm^2. Targeted at this dose, we can optimize the mask CD bias from dense to iso-pitches such that every pitch print the same CD on wafer. Under the optimum biasing condition, different mask absorbers will be compared in terms of DOM, ILS, MEEF, LCDU, CD-DOF, and NILS-DOF.

Figure 9 shows the through-pitch ILS and LCDU for 3 mask absorbers. HR-PSM mask doesn't show better ILS than LnHk mask at minimum pitch. However it starts to increase ILS after 37nm-pitch and maintain such advantage against other absorbers up to the iso-pitch. As for LCDU through-pitch performance, as HR-PSM works with MOR while the other two absorbers with CAR, the fact of larger D2G = 16.5 mj/cm^2 of MOR than D2C = 10 mj/cm^2 of CAR further reduces LCDU of HR-PSM as compared to those of other masks. Figure 10 compares the optimum wafer-scaled DOM and MEEF through-pitch. Contrary to the mask complexity of chromeless-phase lithography (CPL™)[2,3], HR-PSM shows a good proximity effect such that simple mask biasing is adequate to make hole patterns print on target. No sub-resolution assist features is needed. The DOM of HR-PSM ranges from 12 nm to 16 nm, ensuring the image of holes remains in dark spots from dense to isolated pitches. On the other hand, similar to CPL™, HR-PSM has very low MEEF numbers through-pitch, which also implies insensitivity of wafer CD to mask CD noise.

Figure 11 compares the common process window (PW) in terms of NILS-DOF (assuming blurred image NILS ≥ 1.5 is required) and CD-DOF. Obviously, the HR-PSM + MOR approach enlarges the PW in both NILS-DOF and CD-DOF. Figure 12 illustrates the defectivity concern in non-opaque masks. Half-tone HR-PSM is expected to have less phase defects than bright-field binary masks.

Low-k_1 imaging of HR-PSM for CH patterning at 0.33NA EUV

Figure 13 plots the through-pitch exposure dose needed for three absorbers to print with the same

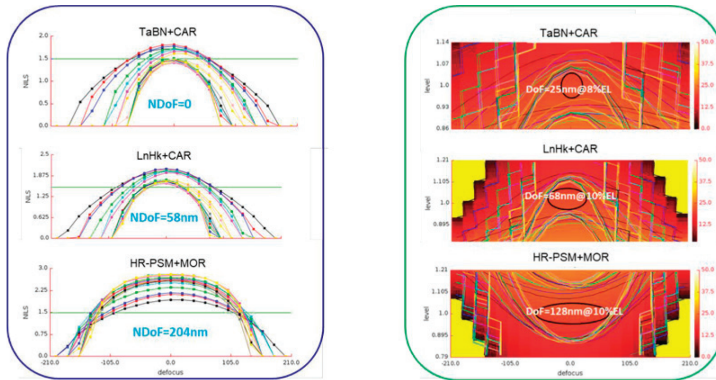

Figure 11. *Comparison of common NILS-DOF (left) and common CD-DOF (right) through pitch for 3 mask absorbers.*

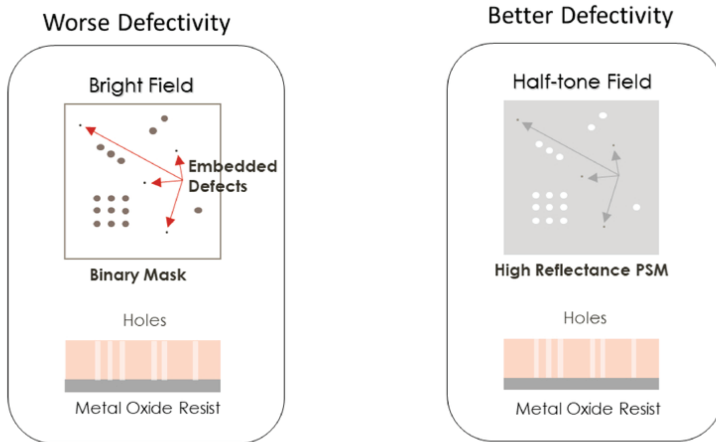

Figure 12. *Phase defects embedded in the bright field mask remain problematic in mask fabrication. HR-PSM with half-tone field is expected to have better defectivity than bright-field binary masks.*

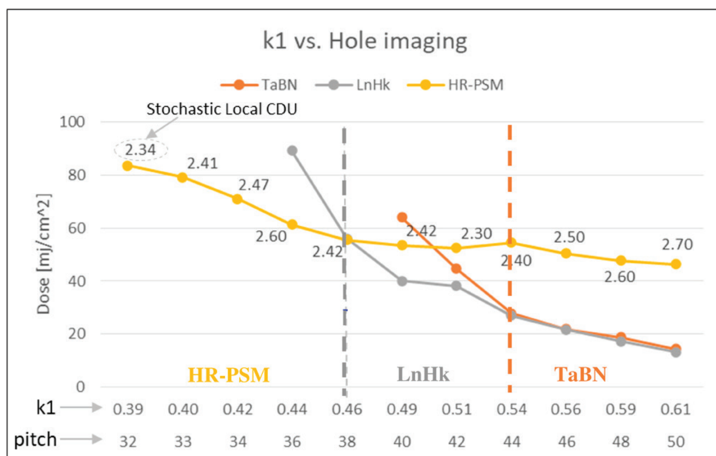

Figure 13. *HR-PSM is a better solution for printing holes at $k_1 < 0.46$ (pitch < 38 nm) using 0.33NA EUVL.*

LCDU (indicated with grey numbers). For the same consideration as above, the target DOW is set to HP + 2 nm. As shown in the graph, TaBN absorber can resolve CH of pitch ≥ 44 nm while LnHk absorber shows dose benefit until $k_1 = 0.46$ (pitch = 38 nm). For $k_1 < 0.46$, HR-PSM starts to show its advantage over the other two absorbers for the single patterning of logic CH. In the figure, LCDU is relaxed starting at the 40-nm pitch to allow for a more reasonable exposure dose. However, regardless of the dose, TaBN can meet the 10% LCDU target down to the 42-nm pitch, LnHk can meet the 10% LCDU target further down to the 40-nm pitch, and HR-PSM can make it even further, down to the 36-nm pitch.

CONCLUSION

The phenomenon of image-tone reversal by changing the mask size has been proved and illustrated for HR-PSM. Based on this effect, we have proposed a novel approach to couple the bright-field image of HR-PSM with the lower resist blur of MOR to form contact holes directly in photoresist without the additional tone-reversal process. Based on wafer-data-calibrated resist models, our simulation assessment for 36nm-minimum-pitch logic CH single patterning has shown that our approach (HR-PSM + MOR) demonstrates superior performance through pitch than TaBN and LnHk mask absorbers in terms of critical imaging metrics such as ILS, LCDU, MEEF, CD-DOF and NILS-DOF, etc. Furthermore, considering the trade-off between LCDU and exposure dose, we have identified that TaBN absorber is able to pattern logic CH until $k_1 = 0.54$. For $0.46 \leq k_1 \leq 0.54$, LnHk may be a good candidate to replace TaBN. Starting from $k_1 = 0.46$ and below, HR-PSM may be best suited for low-k_1 imaging for 0.33NA EUV lithography.

ACKNOWLEDGEMENTS

The authors would like to thank Amrit Narasimhan and Shu-Hao Chang of INPRIA for sharing wafer data and useful discussions on resist. Wei-Min Gao and Tsann-Bim Chiou of ASML TDC are acknowledged for valuable discussions on imaging simulation and resist model calibration.

REFERENCES

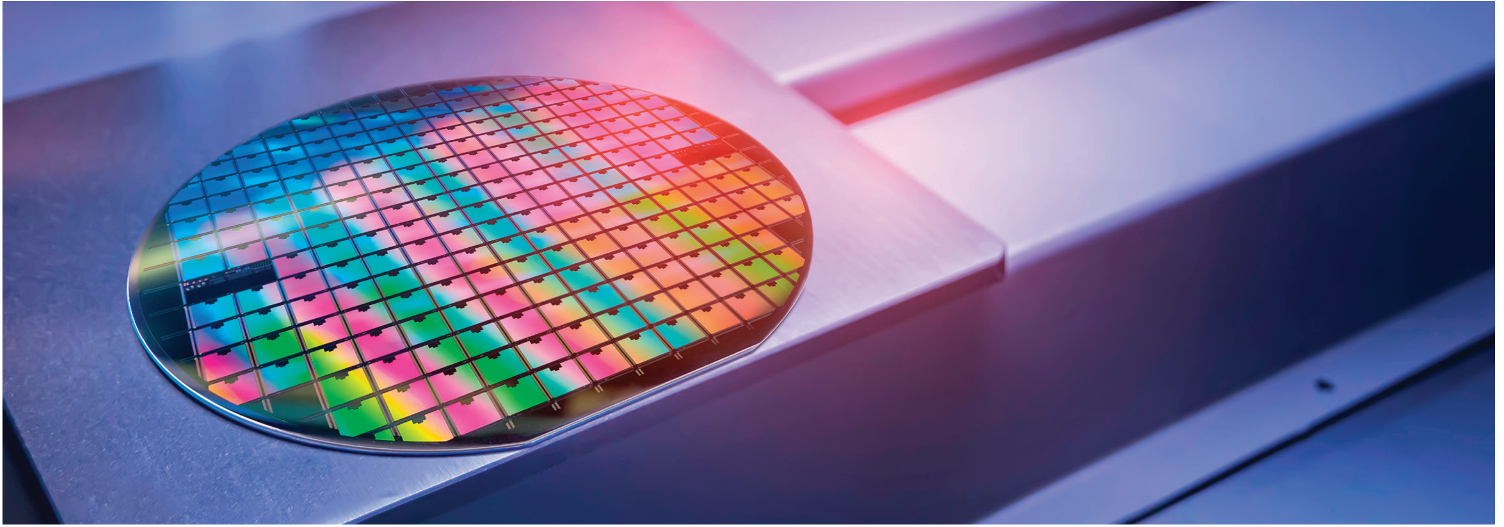

1. Andreas Erdmann, “Optical and EUV Lithography: A Modeling Perspective”, SPIE Press, Bellingham, Washington (2021).
2. Douglas Van Den Broeke et al., “Complex two-dimensional pattern lithography using chromeless phase lithography”, Proc. SPIE 4691, Optical Microlithography XV (2002).
3. Vincent Wiaux et al., “Through pitch low-k_1 contact hole imaging with CPL^{TM} technology”, Proc. SPIE 5446, Photomask and Next-Generation Lithography Mask Technology XI (2004).
4. Claire van Lare et al., “Mask-absorber optimization: the next phase”, J. Micro/Nanolith. MEMS MOEMS Vol. 19(2), 024401 (2020).
5. Chang-Nam Ahn et al., “Optical design of EUV attenuated PSM for contact-hole applications”, Proc. SPIE 11609, 116090D (2021).
6. F. Schleicher et al., "Tone reversal patterning for advanced technology nodes", Proc. SPIE 12056, 1205605 (2022).
7. G. M. Gallatin, “Resist Blur and Line Edge Roughness”, Proc. SPIE 5754, (2005).
8. T. Wallow et al., “Evaluation of EUV resist materials for use at the 32 nm half-pitch node”, Proc. SPIE 6921, 69211F (2008).
9. Zhih-Yu Pan et al., “Influence of shot noise on CDU with DUV, EUV, and E-beam”, Proc. SPIE 6924, 69241K (2008).
10. Seo-Min Kim et al, “EUV stochastic noise analysis and LCDU mitigation by etching on dense contact-hole array patterns”, Proc. SPIE, 9048-9 (2014).
11. Seo-Min Kim et al.,” Understanding of stochastic noise”, Proc. SPIE Vol. 9422, 94220M (2015).
12. Bernd Geh, "EUVL: the natural evolution of optical microlithography", Proc. SPIE 10957, 1095705 (2019).
13. J. G. Santaclara et al., “One metric to rule them all: new k4 definition for photoresist characterization”, Proc. SPIE 11323, 113231A (2020).
14. Wei-Min Gao et al., “Computational lithographic study of 0.55 NA EUV single patterning for metal layers of the 2nm logic node and beyond”, Proc. SPIE 12052, 120520G (2022).

INDUSTRY BRIEFS

High-NA lithography starting to take shape

First systems built, with production planned for 2025; hyper-NA to follow next decade.

The future of semiconductor technology is often viewed through the lenses of photolithography equipment, which continues to offer better resolution for future process nodes despite an almost perpetual barrage of highly challenging technological issues. Those issues have been overcome all the way to the 7nm process node, but a host of new ones are on the horizon, as well as some important improvements.

semiengineering.com

India and Japan to collaborate in building semiconductors and resilient supply chains

Russia's war in Ukraine has disrupted the global supply of parts and raw materials needed to complete a variety of products—from cars to computer chips. India and Japan explored collaborating in critical technologies, including semiconductors and resilient supply chains, as part of plans to reach a target of $35.9 billion Japanese investment in the country by 2027. Foreign Ministers of India and Japan, S. Jaishankar and Yoshimasa Hayashi, met in New Delhi on Thursday and discussed ways to deepen defense equipment and technology cooperation.

msn.com

The US could lose the global chip race without more workers

Washington's semiconductor spending spree isn't working. In the name of competing with China, President Joe Biden signed the Chips and Science Act into law last year. It aims to build a US semiconductor supply chain by providing $52.7 billion for semiconductor research, development, and manufacturing, and workforce development. Private companies have since invested $210 billion in manufacturing across the country, starting 50 new semiconductor projects. But without urgent efforts to increase the number of semiconductor workers in the US, these investments could fail.

msn.com

School for semiconductors? Arm tries to address chip talent shortages

US, Europe and China all rushing to create next gen of experts and upskill existing workforce. Chip designer Arm is looking to address the shortage of vital skills in the semiconductor industry with an initiative that aims to help find the next generation of talent and upskill the existing workforce. The global initiative—the Semiconductor Education Alliance (SEA) – brings together a bunch of like-minded companies from across the industry, all intent on ensuring that a lack of workers with the right expertise does not hinder growth, just when many countries are looking to revitalize their chip industries.

msn.com

ASML, ASM International cut by Bernstein on worries over 'softening demand'

Semiconductor companies ASML Holding (NASDAQ:ASML) and ASM International (OTCQX:ASMIY) shares were downgraded by Bernstein on Friday as the investment firm said there are concerns over "softening demand" for 2023 and 2024.

"We continue to like the fundamentals and growth for both of these companies as we look towards 2025 and beyond," analyst Sara Russo wrote in an investor note. "However, we believe the risk from softening demand for leading edge logic/foundry and ongoing memory weakness now outweighs the upside."

msn.com

MEMBERSHIP

Join the premier professional organization for mask makers and mask users

About the BACUS Group

Founded in 1980 by a group of chrome blank users wanting a single voice to interact with suppliers, BACUS has grown to become the largest and most widely known forum for the exchange of technical information of interest to photomask and reticle makers. BACUS joined SPIE in January of 1991 to expand the exchange of information with mask makers around the world.

The group sponsors an informative monthly meeting and newsletter, BACUS News. The BACUS annual Photomask Technology Symposium covers photomask technology, photomask processes, lithography, materials and resists, phase shift masks, inspection and repair, metrology, and quality and manufacturing management.

Individual Membership benefits include:

- Subscription to BACUS News (monthly)
- Eligibility to hold office on BACUS Steering Committee

Corporate Membership benefits include:

- 3–10 Voting Members in the SPIE General Membership, depending on tier level
- Subscription to BACUS News (monthly)
- One online SPIE journal subscription
- Listed as a Corporate Member in the BACUS News

spie.org/membership/bacus-technical-group

Key Dates

2023

SPIE Photomask Technology + EUV Lithography
1–5 October 2023
Monterey, California, USA
spie.org/puv

2024

SPIE Advanced Lithography + Patterning
25–29 February 2024
San Jose, California, USA
spie.org/al

Photomask Japan
16–18 April 2024
Yokohama, Japan
smartconf.jp

You are invited to submit events of interest for this calendar. Please send to tyb@spie.org.

Sponsorship Opportunities

Sign up now for the best sponsorship opportunities

Photomask Technology + EUV Lithography 2023

Contact:
Melissa Valum, Tel: +1 360 685 5596
melissav@spie.org

Advanced Lithography + Patterning 2024

Contact:
Melissa Valum, Tel: +1 360 685 5596
melissav@spie.org

Kim Abair, Tel: +1 360 685 5499
kima@spie.org

Advertise in the BACUS News

The BACUS newsletter is the premier publication serving the photomask industry. For information on how to advertise, contact:

Melissa Valum, Tel: +1 360 685 5596
melissav@spie.org

BACUS Corporate Members

Acuphase Inc.
American Coating Technologies LLC
AMETEK Precitech, Inc.
Berliner Glas KGaA Herbert Kubatz GmbH & Co.
FUJIFILM Electronic Materials U.S.A., Inc.
Gudeng Precision Industrial Co., Ltd.
Halocarbon Products
HamaTech APE GmbH & Co. KG
Hitachi High Technologies America, Inc.
JEOL USA Inc.
Mentor Graphics Corp.
Molecular Imprints, Inc.
Panavision Federal Systems, LLC
Profilocolore Srl
Raytheon ELCAN Optical Technologies
XYALIS

SPIE.
P.O. Box 10, Bellingham, WA 98227-0010 USA
Tel: +1 360 676 3290
SPIE.org
help@spie.org
©2023

Shipping Address
1000 20th St.,
Bellingham, WA 98225-6705 USA

SPIE is a registered trademark of the Society of Photo-Optical Instrumentation Engineers.
All rights reserved.